Materials Research. 2022; 25:e20210269
DOI: https://doi.org/10.1590/1980-5373-MR-2021-0269

Structural and Magnetic Properties of Ni-doped Yttrium Iron Garnet ($Y_3Fe_{5-X}Ni_xO_{12}$) Nanopowders Synthesized by Self-Combustion Method

Poppy Puspitasari[a,b]*, ***Wahyu Ariffandy[a]***, ***Latief Setyo Budi[a]***, ***Maizatul Shima Shaharun[c]***

[a]Universitas Negeri Malang, Mechanical Engineering Department, Semarang St. No. 5, Malang, East Java, Indonesia.
[b]Universitas Negeri Malang, Center of Advanced Materials and Renewable Energy, Semarang St. No. 5 Malang, East Java, Indonesia.
[c]University Technology Petronas, Fundamental and Applied Science Department, Bandar Seri Iskandar, Perak, Malaysia.

Received: June 07, 2021; Revised: January 2, 2022; Accepted: January 10, 2022

This research aimed to investigate the structural and magnetic properties of Yttrium Iron Garnet by Ni-doped using self-combustion method. Ni-doped directly changed the structure into $Y_3Fe_{5-X}Ni_xO_{12}$ (x=0.00, 0.02, 0.04, 0.06, 0.08). Self-combustion method was obtained by stirring raw materials at room temperature (27°–28°C) and heated at 150°C until combustion occurred. The samples were sintered at 900°C with 120 minutes holding time. The phase identification revealed the cubic structure of garnet phase with the crystallite size from 62.73–62.87 nm. The molecular bonding from molecular bonding displayed Ni-O and Fe-O bonds, while the magnetic properties shown the highest saturation magnetization of 27.04 emu/g in the sample with additional Ni x=0.02, the highest magnetic remenance of 16.09 in the sample Ni x=0.02, and the highest coercivity of 0.029 in the sample with Ni x=0.08. This research, by adding nickel element, shows that the coercivity of $Y_3Fe_{5-X}Ni_xO_{12}$ decreased when the particle size is increased. The increase in Ni concentration as doping material cause the double exchange interaction and affected the lattice parameter, molecular bond, and magnetic properties.

Keywords: *Yittrium iron garnet, Nickel, Phase identification, Molecular bonding, magnetic properties.*

1. Introduction

An improvement for a signal processing device is identified in a radar detecting tool, communication, and instrumentation using a microwave device[1]. Microwave devices often use ferrite material due to its high specific resistance, extraordinary magnetic flexibility, price, and performance.

A good ferrite material used in microwave devices is yttrium iron garnet (YIG), ferromagnetic, that has high electric resistivity, stable high radiation, and relatively low magnetization. YIG has a general crystal structure of $A_3B_5O_{12}$ with the specific formula of $Y_3Fe_5O_{12}$[2,3]. Yttrium iron garnet (YIG) is a cubic ferrite material with la$\bar{3}$d structure[4]. YIG itself consists of three garnet lattices: dodecahedra, octahedra, and tetrahedra[5] as shown in Figure 1. Previous research[6] revealed that another material such as nickel (Ni) can be added into yttrium iron garnet (YIG).

Nickel (Ni) is a ubiquitous doping material since it replaces the Iron (Fe) element in yttrium iron garnet (YIG) that causes a formulaic change from yttrium iron garnet (YIG) into $Y_3Fe_{5-X}Ni_xO_{12}$, apart from omitting oxygen from the lattice. Oxygen lattice vacuum modifies some magnetic properties from the yttrium iron garnet (YIG)[7]. Thus, this research analyzed the magnetic property changes due to the modification in the oxygen lattice after nickel addition. Self-combustion is the most comfortable and a fast method that involves temperature to react and quickly synthesize the powder material. It is a process to create smooth powder by combustion in a heated solution containing a salt of the desired metal which has been mixed with the appropriate fuel. Self-combustion is capable of generating high-quality powder (nanometer-sized), which depends on the preparation and parameter. During self-combustion, which is influenced by the heat of the combustion process, physical properties are obtained by the material, including phase purity, particle size, surface area, and agglomeration[8].

Other researcher varied the additional nickel (x = 0.05, 0.1 and 0.2) using citrate combustion method because it enhance the magnetic saturation and decrease the coercivity of YIG ($Y_3Fe_5O_{12}$)[9]. Another study of YIG using ball milling method was done by varying sintering temperatures that resulting the enhancement of magnetic saturation due to the grain size improvement[10]. However, this research observed the influence of nickel doped (x = 0.00, 0.02, 0.04, 0.06, 0.08) to the physical and magnetic properties of YIG.

---

*e-mail: poppy@um.ac.id

Table 1. Research Design Variations.

Sample Material@5g	Amount				
	Yttrium(III) *nitrate hexahydrate*	*Iron*(III) *Nitrate Nonahydrate*	*Nickel*(III) *Nitrate Hexahydrate*	*Distilled Water*	*Citric Acid*
$Y_3Fe_5O_{12}$	2.8247 g	4.9654 g	0 g	50 ml	1 g
$Y_3Fe_{4.98}Ni_{0.02}O_{12}$	2.8264 g	4.9484 g	0.0143 g	50 ml	1 g
$Y_3Fe_{4.96}Ni_{0.04}O_{12}$	2.828 g	4.9314 g	0.0286 g	50 ml	1 g
$Y_3Fe_{4.94}Ni_{0.06}O_{12}$	2.8297 g	4.9144 g	0.0429 g	50 ml	1 g
$Y_3Fe_{4.92}Ni_{0.08}O_{12}$	2.8313 g	4.8973 g	0.0573 g	50 ml	1 g

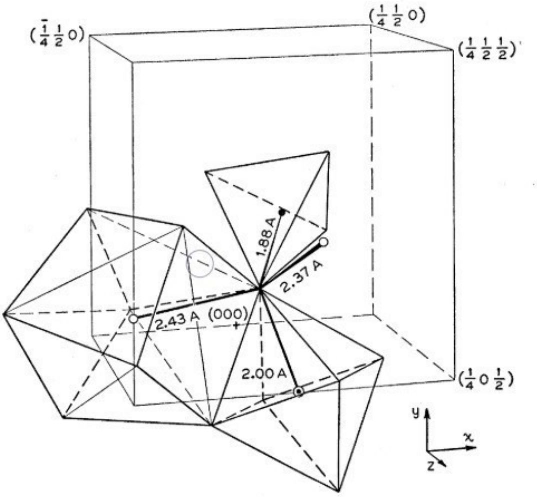

Figure 1. Structure of yttrium iron garnet (YIG) lattice with dodecahedra, octahedra, and tetrahedra from larger to smaller-size order[6].

2. Materials and Methods

2.1. Material preparation

Base material in this research was Yttrium(III) nitrate hexahydrate ($Y(NO_3)_3.6H_2O$), from Sigma Aldrich with the purity of 99.8% and density 26.82 g/ml, Iron(III) nitrate nonahydrate ($Fe(NO_3)_.9H_2O$) with 99% purity and 900 h/m^3 density, and Nickel (III) nitrate hexahydrate ($Ni(NO_3)_2.6H_2O$) with 99% purity and 800 g/ml density from Merck. This research used a solvent from citric acid ($C_6H_8O_7.H_2O$) and distilled water mix. We prepared 50 ml of distilled water and measured the weight of raw material with the composition specified in Table 1. Then, we mixed them in a beaker glass and entered the self-combustion method. The substituted Yttrium Iron Garnet formula by Ni-doping has follow the super exchange theory brought by the work of Agarwal et al.[9]. The suitable formula is :

$$\left\{\boldsymbol{Y}^{3+}\right\}\left[\boldsymbol{Fe}_2^{3+}\right]\left(\boldsymbol{Fe}_3^{3+}\right)\boldsymbol{O}_{12}^{2-} \tag{1}$$

Where the brackets { } denote dodecahedral “c” sites, [ ] denote octahedral “a” sites, and ( ) denote tetrahedral “d” sites. The substitution of magnetic and non magnetic ions on YIG, distorts the crytal structure, Krishnan et al. described that Ni^{2+} ions able to substitute both the tetrahedral and octahedral iron sites[11].

From the garnet structure, it is well known that an octahedral and a tetrahedral ion are linked with each other only once through the oxygen ion, that means each oxygen ion is coordinated with only one each of the octahedral and tetrahedral ions. Therefore, for each of the two octahedral iron ions there are six linkages with tetrahedral ions for a total of twelve, and for each of the tetrahedral ions there are four linkages with octahedral ions for a total of twelve. Consequently there are 24/5 linkages per iron ion in yttrium-iron garnet[12].

2.2. Self-combustion method

The self-combustion method was chosen to carry out this research due to its ease of operation and also more efficient synthesis process compared to co-precipitation, hydrothermal, and pulse laser deposition methods[13-15]. It was performed by dissolving the base material into the solvent with composition, as seen in Table 1. The combination was done using a magnetic stirrer at room temperature for 60 minutes and at 200 rpm speed. The solution was heated at 150 °C temperature until combustion in a beaker glass dried and turned into reddish-brown. The dried gel when heated in an open air underwent a self-propagating and intense exothermic reaction between nitrate and citrate ions[16,17]. The samples underwent a drying process at 150°C and crushed for 60 minutes. After crushing, the samples were sintered at 900 °C in 120 minutes holding time and experienced the second crushing for 60 minutes. The schematic diagram of Nitrate-Citrate mechanism shows in Figure 2.

2.3. Characterization

After obtaining the synthesized powder, the sample was characterized. Phase identification used the X-ray Diffraction (XRD) under the brand of Malvern Pan Analytical (UK) with Cu Kα (λ = 1.54252 Å) in the range 2 theta of 10-90^o with step mode of 0.2^o/min . The crystallite size has been calculated from X-Ray line broadening using Scherer fromula. Morphology identification used the Scanning Electron Microscope (SEM) of Phenom from Thermo Fisher Scientific (USA) with 50K magnification. Functional group tests used the Fourier-transform Infrared Spectroscopy (FTIR) spectrometers of Shimadzu (Japan) with the range of wavelength 500-4000 cm^{-1}. The magnetic properties were tested using the Vibrating Sample Magnetometer (VSM) of

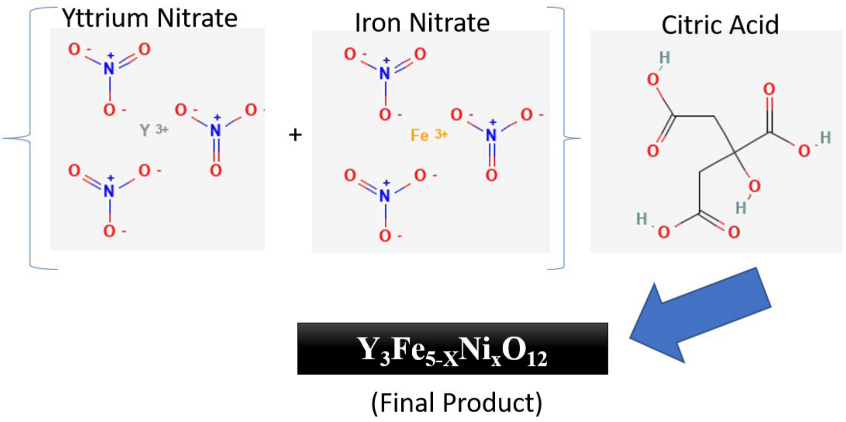

Figure 2. Schematic Diagram of Nitrate-Citrate Mechanism[18-20].

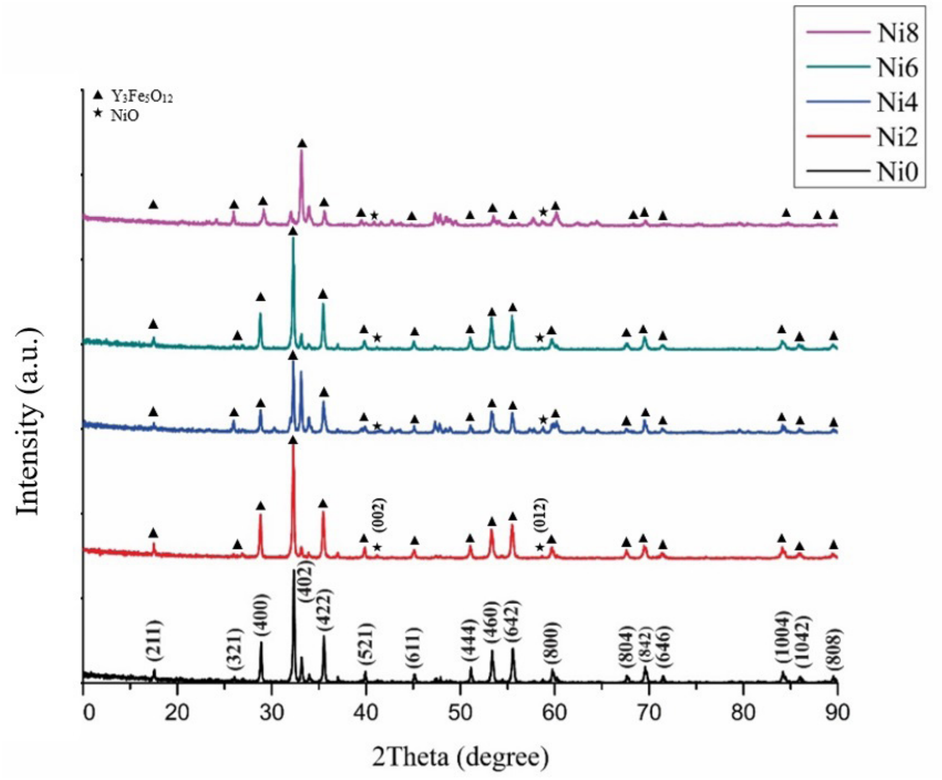

Figure 3. Phase identification of Yttrium Iron Nickel Garnet (YIG) in various composition.

Oxford Instruments 1.2H (UK) at room temperature with magnetic field range of -1–1 Tesla.

3. Results and Discussion

3.1. Phase characterization

Combined phase analysis used diffractogram values and data from the Crystallography Open Database (COD) with the database in this study based on COD-Inorg REV248644. The garnet structure has pure single-phase $Y_3Fe_5O_{12}$ and belongs to the Ia3d group[7,21].

Highest peak on this XRD graph (Figure 3) for all samples is about 32—33 2 theta, which means that (402) hkl index used as base crystallite size (*D*) calculation with Scherrer equation[22].

$$D = \frac{k \times \lambda}{FWHM \times \cos\theta} \tag{2}$$

where D is the mean crystallite size, k (0.89) is the Scherrer constant, λ is X-ray wavelength (0.154252 nm), and β is the relative value of the full width at half maximum (FWHM) of the diffraction peak (402). Apart from the phase, the crystallite size was obtained from X-ray Diffraction (XRD)[23]. We obtained this value using the Scherrer Equation[24,25]. Ni concentration as doping nanoparticles, also called as the impurity to the host ions. To incorporate impurities into the host lattice, a common route is to adopt the doping ions with the sampe valence and the similar radii to the ones in the hosts. The possible changes in the crystal lattice after impurity doping will cause the crystal lattice expance[26].

Based on Table 2, the smallest crystallite sixes are $Y_3Fe_{4.98}Ni_{0.02}O_{12}$ and $Y_3Fe_{4.92}Ni_{0.08}O_{12}$ with 62.73 nm, while the largest size is $Y_3Fe_{4.94}Ni_{0.06}O_{12}$ with 62.87 nm. Normally, the resulting size of this study leads a decreasing crystallite size because the size of Fe with an ionic radius of 74 pm is replaced by Ni with an ionic radius of 69 pm[27]. However, this is not applied since the sintering temperature is the same as each sample. The decrease in the crystallite size are attributed to the substitution of Fe cation by Ni ions. Ni ions are succesfully incorporated into the ferrite and restrict the grain growth which result the slightly decrease of crystallite size[28].

An enlargement of the crystallite size occurred in the sample $Y_3Fe_{4.94}Ni_{0.06}O_{12}$, called a deviation. This was due to distortion as oxygen vacancies increase and reduce the Full-width half maximum (FWHM) value of the material. This causes the value of the peak position to be low compared to other samples. This is reinforced by the Scherrer equation where the crystallite size is inversely proportional to the peak position of the phase[29]. The value of lattice parameter gradually decrease with respect to Ni concentration which is attributed to the ionic radii of the respective ions ferrites. This result was consistent with the research of[30]. The similar behaviour found for the changes of X-ray density on garnet $Dy_3Fe_{5-x}Mn_xO_{12}$[28] and $Dy_{2.8}Sr_{0.2}Fe_5O_{12}$ via citrate auto combustion[31].

3.2. Morphological characterization

Figure 4 shows that the addition causes the grains to aggregate but still spread evenly, and with this magnification, the shape and size of the sample grain can be seen. It is observed directly that the size comparison from Figures 3a to 3e has a relatively insignificant difference in grain size and has a different level of grain shape homogeneity. The difference in size is due to Ni-doped which has shown that Ni0.08 has the largest grain size, denser structure and fewer defect[32].

The grain size produced in this synthesis can provide a nanometer size dominated by micrometer-sized granules. This result occurs in almost all samples and the grain sizes of nanometers also spread evenly. This is because nickel, which functions to replace iron, does not significantly change the morphology of yttrium iron particles[7].

3.3. Fourier-transform infrared spectroscopy (FTIR) analysis

There are five functional group bonds with different regions in Figure 5 which are a graph of the Fourier-transform infrared spectroscopy (VS) results of yttrium iron nickel garnet. It shows that there are five functional group bonds in the $Y_3Fe_{5-x}Ni_xO_{12}$ sample (x = 0.00, 0.02, 0.04, 0.06, 0.08).

Sample is seen through a valley where the difference is not too significant. Region I contains a valley with each sample from $Y_3Fe_{5-x}Ni_xO_{12}$ (x = 0.00, 0.02, 0.04, 0.06, 0.08) 3446.79419 cm^{-1}, 3442.93656 cm^{-1}, 3442.93656 cm^{-1}, 3446.79419 cm^{-1}, 3442.93656 cm^{-1}. Previous research by Tholkapiyan et al.[30] uncovered that the wavelength of 3550-3200 is a bond of the O-H functional group with the stretching group, which has a strong and broad appearance that enters the alcohol group of compounds with intermolecular bonds. The frequency band in the range between 3200-3600 cm^{-1} is attributed to O-H stretching vibration of water molecules adsorbed during the exposure of dried powder to air.

Region III contains a valley with each sample from $Y_3Fe_{5-x}Ni_xO_{12}$ (x = 0.00, 0.02, 0.04, 0.06, 0.08) respectively 1637.56478 cm-1, 1631.77834 cm-1, 1631.77834 cm-1, 1637.56478 cm-1, 1639.4936 cm-1. It corresponds to the previous research by Adenkule et al.[33] who revealed that wavelength 1648-1638 is a a stretching band of C = C bond with a strong bond appearance and is included in the alkene class. This compound is derived from citric acid compounds as a combustion material that is not completely lost.

Region IV contains a valley with each sample of $Y_3Fe_{5-x}Ni_xO_{12}$ (x = 0.00, 0.02, 0.04, 0.06, 0.08) 1386.8187 cm^{-1}, 1384.88989 cm^{-1}, 1384.88989 cm^{-1}, 1384.88989 cm^{-1}, 1384.88989 cm^{-1}, respectively. Previously, Adenkule et al.[33] have explained that the wavelength of 1420-1330 cm^{-1} is an O-H bond with a bending bond entering into alcohol class with medium bond strength. The O-H bonds in regions I and IV indicate that the water compound is not completely lost even though some heat treatment is carried out on the sample. The range of 500-600 cm^{-1} revealed the formation of garnet structure ($Y_3A_2B_3O_{12}$) having octahedral and tetrahedral ions disturbed over A-sites and B-sites, respectively[28]. Absorption bands at 450-600 cm^{-1} revealed the single phase garnet structure and this region consists of Metal-O stretching vibration in tetrahedral site[30].

Region IV also contains peaks from $Y_3Fe_{5-x}Ni_xO_{12}$ (x = 0.00, 0.02, 0.04, 0.06, 0.08) with positions in the order of 650.01099 cm^{-1}, 648.08218 cm^{-1}, 650.01099 cm^{-1}, 651.93981 cm^{-1}, 694.37376 cm^{-1}. Previous research by Fechine et al.[34] showcases that the wavelength range of 610-664 cm^{-1} is a

Table 2. Phase Identification results from XRD.

Sample Material	*Position* [°]	*D-spacing* [Å]	*Crystallite Size* [nm]
$Y_3Fe_5O_{12}$	32.3551	2.7670	62.74
$Y_3Fe_{4.98}Ni_{0.02}O_{12}$	32.2932	2.7722	62.73
$Y_3Fe_{4.96}Ni_{0.04}O_{12}$	32.3013	2.77323	62.74
$Y_3Fe_{4.94}Ni_{0.06}O_{12}$	32.2808	2.77152	62.87
$Y_3Fe_{4.92}Ni_{0.08}O_{12}$	33.1515	2.70236	62.73

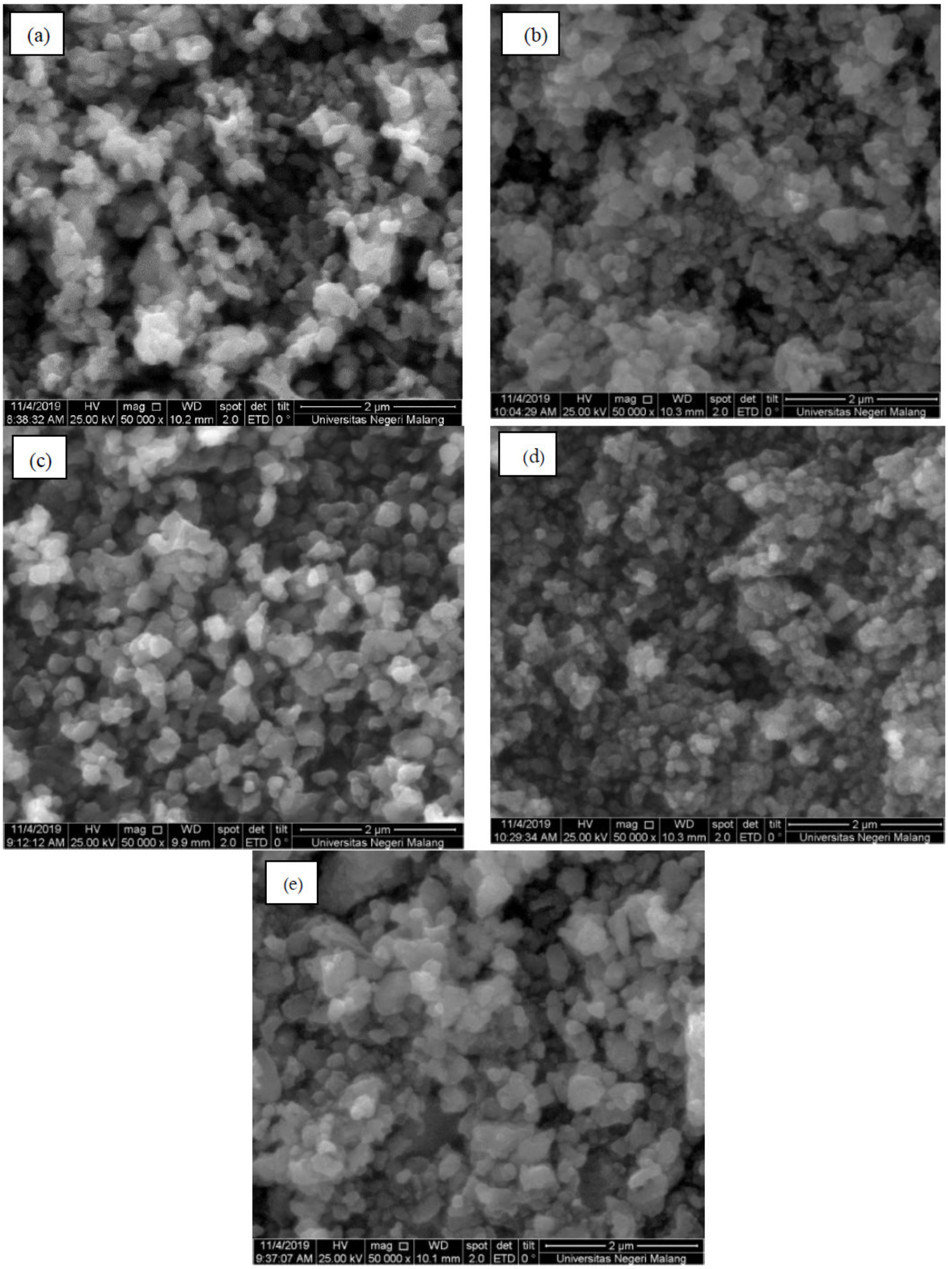

Figure 4. Morphology of Yttrium Iron Garnet with nickel a) Ni0.00, b) Ni0.02, c) Ni0.04, d) Ni0.06 and e) Ni0.08 in 50.000x magnification.

functional group bond of Fe-O with a strong bond and is known to have an octahedral lattice[33-35].

In region IV, peaks with wavenumber positions are 457.12939 cm^{-1}, 453.27176 cm^{-1}, 455.20058 cm^{-1}, 457.12939 cm^{-1}, 457.12939 cm^{-1} in sequence. In a similar vein, Vladár and Hodoroaba[36] revealed that in the wavelength range of 454-474.5 cm^{-1} is a functional group bond of Ni-O, showing that Nickel has succeeded in becoming a substitute in the material of $Y_3Fe_{5-x}Ni_xO_{12}$[36,37]. The bond of Fe-O and Ni-O compounds is the identity or fingerprint compound of the $Y_3Fe_{5-x}Ni_xO_{12}$ absorption band (x = 0.00, 0.02, 0.04, 0.06, 0.08). The reduction in the intensity peak and also the shifted of frequency because of the increasing Ni concentration. This is due to the Ni atoms occupying octahedral sites of Fe ions and pushing Fe ions towards oxygen ion[30].

3.4. Magnetic properties analysis

The resulting hysteresis curve in Figure 6 has a narrow gap and a saturation value above 0.5 Oe (equivalent to 0.00005 T)[7]. Based on this statement, the $Y_3Fe_{5-x}Ni_xO_{12}$ sample (x = 0.00, 0.02, 0.04, 0.06, 0.08) is included in soft magnetic materials (Pena-Garcia et al.[38]) Based on Figure 6, its magnetic characteristics can be analyzed using Magnetic Saturation (Ms), Magnetic remanence (Mr), and coercivity (Hc) presented in Table 3 which are obtained based on the approach of the hysteresis curve. The saturation magnetization

Table 3. Magnetic Saturarion (Ms), Magnetic Remenance (Mr), and Coercivity (Hc) from Hysteresis Loop.

Sample Material	Ms [emu/g]	Mr [emu/g]	Hc [T]
$Y_3Fe_5O_{12}$	23.684	13.62	0.021
$Y_3Fe_{4.98}Ni_{0.02}O_{12}$	27.039	16.09	0.02034
$Y_3Fe_{4.96}Ni_{0.04}O_{12}$	18.825	9.36	0.0234
$Y_3Fe_{4.94}Ni_{0.06}O_{12}$	26.924	14.89	0.021
$Y_3Fe_{4.92}Ni_{0.08}O_{12}$	2.518	1.13	0.029

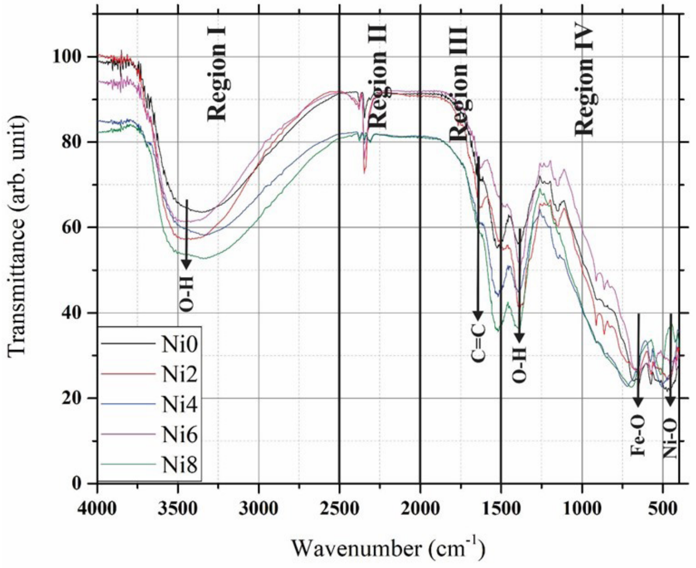

Figure 5. Molecular bonding of Yttrium Iron Nickel Garnet.

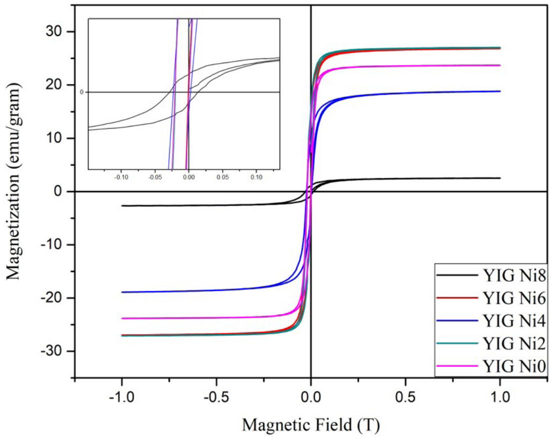

Figure 6. The hysteresis curve of $Y_3Fe_{5-x}Ni_xO_{12}$ (x= 0.00, 0.02, 0.04, 0.06, and 0.08).

(Ms) value for pure YIG nanoparticles was 23.684 emu/g. This is higher value than previously reported for DIG (8.29 emu/g) and Y3Fe5-xAlxO12 (6.97-0.308)[30]. The magnetic moment of Fe ions at the tetrahedral site is antiparallel and coupled to the octahedral site through super exchange interaction, wthich result the net magnetic moment. The increase of Ni concentration leading to increases of saturation magnetization (Ms) value because of a double exchange interaction. This interaction can induce cation ordered distribution in the octahderal site and resulting ferromagnetic behaviour[30].

Xavier et al. in[27] contended that the magnetic characteristics of a material are related to and influenced by the crystallite size of the material obtained from x-ray diffraction (XRD) through the Scherrer equation. However, this research shows that nickel doping has not effected the crystallite size value. Therefore, this section specifically explains the effect of nickel dopping on the Magnetic Saturation (Ms), Magnetic remanence (Mr), and coercivity (Hc) values in the $Y_3Fe_{5-x}Ni_xO_{12}$ material (x = 0.00, 0.02, 0.04, 0.06, 0.08).

Based on the comparison of Ms and H_C to nickel composition, Ms value is inversely proportional to the value of Hc. This statement is supported by the Brown's Equation[39,40].

$$H_c = \frac{2K_1}{\mu_0 M_s} \tag{3}$$

Figure 7 presents the Ms value of raw material with Ms of 23.684 emu/g, while this research was to observe changes in samples doped with Ni. Ms reaches the maximum value in the sample x = 0.02 with a value of 27.039 emu/g, x = 0.04. It produces a value of 18.825 emu/g, x = 0.06 which is 26.924 emu/g and also the minimum value which is obtained at x = 0.08 is 2.518 emu/g. This value of Ms is generated from the anti-parallel coupling between the two magnetic sub-lattices for the octahedral (16 *a*-sites) and the tetrahedral (24 *d*-sites) positions filled with Fe^{3+} ions. According to the analysis of Figure 8 the structure of Ni ion is located in the octahedral and tetrahedral sites. Theoretically, the substitution of iron with nickel at the site reduces the YIG total magnetic moment. This happened at x = 0.02, 0.04, and 0.08. Besides, Ni can also increase the value of Ms, such as the phenomenon at x = 0.06 due to the oxygen void caused by the presence of nickel. There is a strong spontaneous interaction between the oxygen vacancies and the magnetic ion in the octahedral lattice (Fe and Ni) that eliminates thermal effects and increases the sub-grid magnetic moment of the octahedral[38]. The very low Ms value at x = 0.08 with a value of 2.518 emu/g can be attributed to the spin canting mechanism where the substitution of Ni ions causes non-collinear spin changes, which lead to crystal lattice irregularities[7,25,38]. This causes some sites to have no ion interactions and causes the Ms value to decrease.

The magnetic remanence (Mr) value strongly depends on the Ni concentration and the same factor effect as the magnetic saturation (Ms). It can be seen in Figure 9 The fluctuation that occurs is similar to the state of Ms with a maximum remanence value of 16.04 emu/g at x = 0.02 and a minimum value of 1.13 emu/g at x = 0.08. Previous research explored the increase of Ni concentration and Ni atoms that can come close to each other. This implies the presence of some Ni^{2+} ions with Ni^{2+} nearest neighbors[26]. Increasing Ni concentration will increase the volume fraction of Ni^{2+} ions. The super exchange interaction between these Ni^{2+} ions is responsible for ferromagnetism[41,42,43,44]. Thus, the reduction of saturation and remanence magnetization in our samples are due to the enhanced antiferromagnetic interaction.

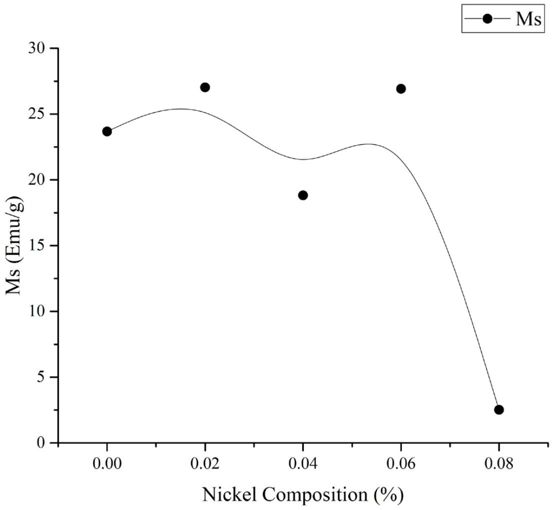

Figure 7. Comparison magnetic saturation (Ms) with Nickel Composition $Y_3Fe_{5-x}Ni_xO_{12}$ (x= 0.00, 0.02, 0.04, 0.06, and 0.08).

Figure 10 shows that high coercivity (Hc) for x = 0.00 is 0.021 T and 0.02034 T for x = 0.02. The crystallite size for x = 0.00 is 62.74 nm and 62.73 nm for x = 0.02. Furthermore, the critical size for the single domain configuration at YIG is 35 nm, so that an increase in Hc is expected, but the opposite happens because the spin canting mechanism (Figure 10) destroys the single domain configuration locally and causes a decrease in the coercivity value to 0.02034 T[7]. The Hc value of ferrite nanoparticles depends on the micro-strain, inter-particle interaction, magneto-crystalline anisotropy, particle size, and morphology[28,]. The decreasing of Hc value with increasing Ni concentration due to the porosity. Porosity affects magnetization process because pores work as a generator of demagnetizing field. The porosity decrease leads to lower values of the coercive field[28,41].

The same argument is applied to x = 0.04 and x = 0.06 where the sizes of 62.74 nm and 62.87 nm cause fluctuations of Hc to 0.0234 T and 0.021 T, with the crystallite size which is quite significant at x = 0.06. Another mechanism appears and causes fluctuation, magnetic moments that appear at x = 0.06. x = 0.08 indicates a decrease in the crystallite size to 62.73 nm and an increase in Hc value to 0.029 T. This finding is consistent with the statement that

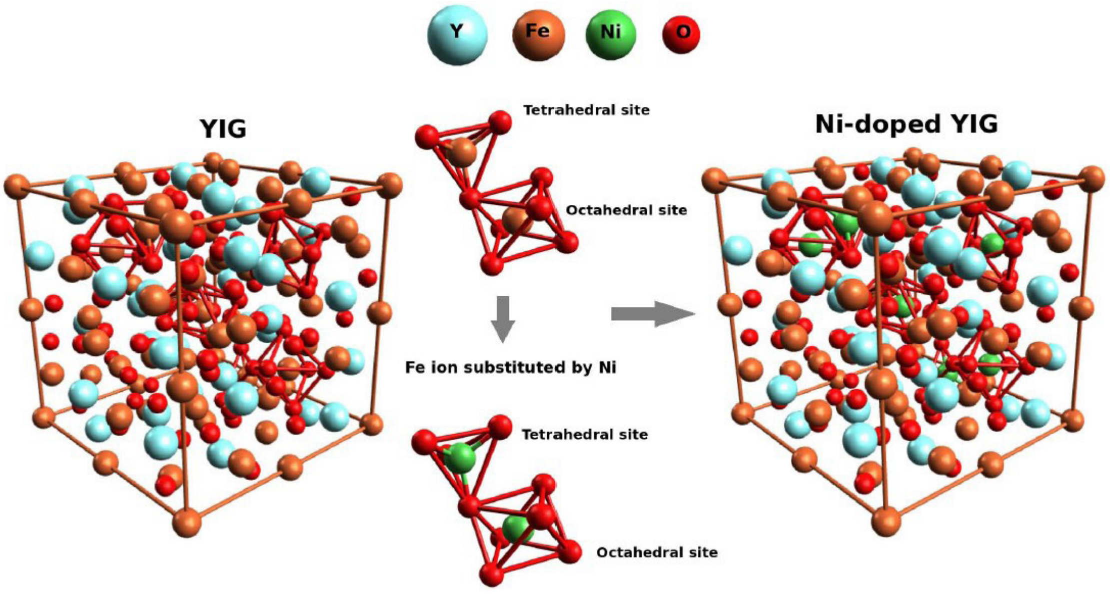

Figure 8. Illustration of the substitution of Fe and Ni atoms in the Tetrahedral and Octahedral Lattices[7].

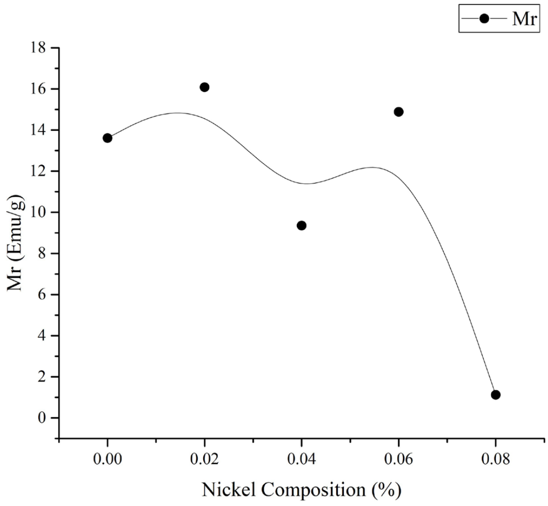

Figure 9. Comparison magnetic remanence with nickel composition $Y_3Fe_{5-x}Ni_xO_{12}$ (x= 0.00, 0.02, 0.04, 0.06, and 0.08)**.**

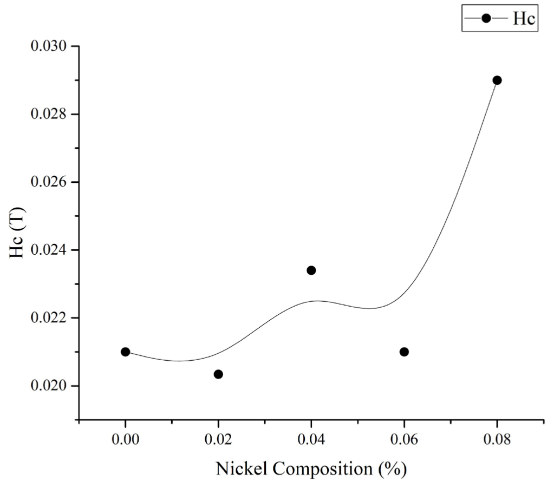

Figure 10. Comparison coercivity with nickel composition $Y_3Fe_{5-x}Ni_xO_{12}$ (x= 0.00, 0.02, 0.04, 0.06, and 0.08).

when the crystallite size approaches the critical size, the Hc value increases[28,45].

4. Conclusion

This research has successfully performed $Y_3Fe_{5-x}Ni_xO_{12}$ (x = 0.00, 0.02, 0.04, 0.06, 0.08) magnetic material synthesis based on the analysis and material testing using several characterizations. The XRD analysis also showed that the magnetic material has a single phase with the highest peak having an hkl index [402] with a position range of 32-33°. Besides, it has a crystallite size of nanometer size with a size range of 62.73-62.87nm. The grains obtained in this research are aggregated and have an even distribution. These can produce nanometer grain size, albeit micrometer-sized grains are dominating. Our research also successfully generated Fe-O bonds in the wavelength range of 648-694cm^{-1} and Ni-O in the wavelength range of 453-457cm^{-1}. These two bonds appear because Fe is the main element in the YIG material and Ni is its substitute. Based on the magnetic characteristics, the best samples which has excellent Ms, Mr, and Hc, is $Y_3Fe_{5-x}Ni_xO_{12}$ with Ni = 0.02.

5. References

1. Abdullahi M, Azis S, Huda N, Hassan J. Structural and magnetic properties of yttrium iron garnet (YIG) and yttrium aluminum iron garnet (YAlG) nanoferrite via sol-gel synthesis. Results Phys. 2017;7:1135-42. http://dx.doi.org/10.1016/j.rinp.2017.02.038.
2. Niyaifar M, Mohammadpour H, Dorafshani M, Hasanpour A. Size dependence of non-magnetic thickness in YIG nanoparticles. J Magn Magn Mater. 2016;409:104-10. http://dx.doi.org/10.1016/j.jmmm.2016.02.097.
3. Puspitasari P, Doko A, Ekaputri JJ, Risdanareni P. Properties of $Y_3Fe_5O_{12}$ (YIG) as nanocatalyst for ammonia formation produced from Magnetic Induction Method (MIM). Mater Sci Forum. 2016;857:146-50. http://dx.doi.org/10.4028/www.scientific.net/MSF.857.146.
4. Anupama AV, Kumar R, Kumar H, Sahoo B. Synthesis of coral-shaped yttrium-aluminium-iron garnets by solution-combustion method. Ceram Int. 2017;44(3):3024-31. http://dx.doi.org/10.1016/j.ceramint.2017.11.059.
5. Gillro MA, Geller S. Magnetic and crystallographic of substitued yttrium-iron garnet, $3Y_2O_3.xM_2O_3(5-x)Fe_2O_3$. Phys Rev. 1958;110:73-8.
6. Leal LRF, Guerra Y, Rodrigues AR, Santos FEP, Peña-Garcia R. Structural and magnetic properties of yttrium iron garnet nanoparticles doped with copper obtained by sol gel method. Mater Lett. 2018;236:547-9. http://dx.doi.org/10.1016/j.matlet.2018.11.004.
7. Peña-Garcia R, Guerra Y, Santos FEP, Almeida LC, Padrón-Hernández E. Structural and magnetic properties of Ni-Doped yttrium iron garnet nanopowders. J Magn Magn Mater. 2019;492;165650. http://dx.doi.org/10.1016/j.jmmm.2019.165650.
8. Chauhan L, Shukla AK, Sreenivas K. Properties of $NiFe_2O_4$ ceramics from powders obtained by auto-combustion synthesis with different fuels. Ceram Int. 2016;42(10):12136-47. http://dx.doi.org/10.1016/j.ceramint.2016.04.146.
9. Agarwal P, Khanduri H, Link J, Stern R, Khand SA, Garg V, Dimri MC. Structural, microstructural, and magnetic studies of Y3Fe5-xNixO12 garnet nanoparticles. Ceram Int. 2020;46(13):21039-45. http://dx.doi.org/10.1016/j.ceramint.2020.05.175.
10. Rodziah N, Hashim M, Idza IR, Ismayadi I, Hapishah AN, Khamirul MA. Applied Surface Science Dependence of developing magnetic hysteresis characteristics on stages of evolving microstructure in polycrystalline yttrium iron garnet. Appl Surf Sci. 2012;258(7):2679-85. http://dx.doi.org/10.1016/j.apsusc.2011.10.117.
11. Krishnan R. Influence of tetrahedral Ni2+ ions on the magnetic properties of YIG. Phys Stat Sol. (b). 1966;18(1):K53-6. http://dx.doi.org/10.1002/pssb.19660180158.
12. Gilleo MA. Superexchange interaction in ferrimagnetic garnets and spinels which contain randomly incomplete linkages. J Phys Chem Solids. 1960;13(1):33-9. http://dx.doi.org/10.1016/0022-3697(60)90124-4.
13. Ibrahim NB, Edwards C, Palmer SB. Pulsed laser ablation deposition of yttrium iron garnet and cerium-substituted YIG films. J Magn Magn Mater. 2000;2-3:183-94.
14. Cho YS, Burdick VL, Amarakoon VRW. Hydrothermal preparation and morphology characteristics of Y3Fe5O12. *J Am Ceram Soc.* 1997;80(6):1605-1608. https://doi.org/10.1111/j.1151-2916.1997.tb03025.x.
15. Rashad MM, Hessien MM, El-Midany A, Ibrahim IA. Effect of synthesis conditions on the preparation of YIG powders via co-

precipitation method. J Magn Magn Mater. 2009;321(22):3752-7. http://dx.doi.org/10.1016/j.jmmm.2009.07.033.

16. Peng C, Zhang Y, Cheng ZW, Cheng X, Meng J. Nitrate-citrate combustion synthesis and properties of Ce_{1-x} $Sm_xO_{2-x/2}$ solid solutions. J Mater Sci Mater Electron. 2002;13:757-62.
17. Banerjee S, Kumar A, Sujatha Devi P. Preparation of nanoparticles of oxides by the citrate–nitrate process: effect of metal ions on the thermal decomposition characteristics. J Therm Anal Calorim. 2011;104(3):859-67. http://dx.doi.org/10.1007/s10973-011-1525-6.
18. National Center for Biotechnology Information. Yttrium nitrate [online]. Bethesda: NBCI; 2021 [cited 2021 Jun 2]. Available from: https://pubchem.ncbi.nlm.nih.gov/compound/Yttrium-nitrate
19. National Center for Biotechnology Information. Ferric nitrate [online]. Bethesda: NBCI; 2021 [cited 2021 Jun 2]. Available from: https://pubchem.ncbi.nlm.nih.gov/compound/Ferric-nitrate
20. National Center for Biotechnology Information. Citric acid [online]. Bethesda: NBCI; 2021 [cited 2021 Jun 2]. Available from: https://pubchem.ncbi.nlm.nih.gov/compound/Citric-acid
21. Baños-l E, Jes S, Cort CA. Enhancement in curie temperature of yttrium iron garnet by doping with neodymium. Materials (Basel). 2018;11:1-12. http://dx.doi.org/10.3390/ma11091652.
22. Cullity BD. Elements of X-ray diffraction. 2nd ed. Boston: Addison Wesley.
23. Epp J. X-Ray Diffraction (XRD) techniques for materials characterization. In: Hübschen G, Altpeter I, Tschuncky R, Herrmann H-G, eds. USA: Elsevier Ltd; 2016. http://dx.doi.org/10.1016/B978-0-08-100040-3.00004-3.
24. Razak JA, Sufian S, Puspitasari P. Synthesis, characterization and application of Y3Fe5O12 nanocatalyst for green production of NH3 using Magnetic Induction Method (MIM) synthesis, characterization and application of Y3Fe5O12 nanocatalyst for green production of NH3 using magnetic indu. AIP Conf Proc. 2012;1482:633. http://dx.doi.org/10.1063/1.4757548.
25. Yahya N, Puspitasari P. $Y_3Fe_5O_{12}$ nanocatalyst for green ammonia production by using magnetic induction method. J Nano Res, 2012;21:131-7. http://dx.doi.org/10.4028/www.scientific.net/JNanoR.21.131.
26. Chen D, Wang Y. Impurity doping: a novel strategy for controllable synthesis of functional lanthanide nanomaterials. Nanoscale. 2013;5(11):4621. http://dx.doi.org/10.1039/c3nr00368j.
27. Xavier PAF, Nair SS, Anantharaman MR. Effect of nickel doping on structural and magneto-optical properties of Fe_3 O_4 ferrofluids. Mater Today: Proc. 2020;25(Pt 2):218-23. http://dx.doi.org/10.1016/j.matpr.2020.01.039.
28. Rekha G, Tholkappiyan R, Vishista K, Hamed F. Systematic study on surface and magnetostructural changes in Mn-substituted dysprosium ferrite by hydrothermal method. Appl Surf Sci. 2016;385:171-81. http://dx.doi.org/10.1016/j.apsusc.2016.05.092.
29. Sattibabu B, Rao TD, Bhatnagar AK, Murthy VS, Chelvane JA, Rayprol S. Structural and magnetic properties of Bi substituted nickel ferrite. Mater Today: Proc. 2020;39(Pt 4):1482-6. http://dx.doi.org/10.1016/j.matpr.2020.05.371.
30. Tholkappiyan R, Vishista K. Tuning the composition and magnetostructure of dysprosium iron garnets by Co-substitution: an XRD, FT-IR, XPS and VSM study. Appl Surf Sci. 2015;351:1016-24. http://dx.doi.org/10.1016/j.apsusc.2015.05.193.
31. Ahmed MA, Bishay ST, El-dek SI. Conduction mechanism and magnetic behavior of dysprosium strontium iron garnet (DySrIG) nanocrystals. Mater Chem Phys. 2011;126(3):780-5. http://dx.doi.org/10.1016/j.matchemphys.2010.12.044.
32. Morais A, Torquato RA, Silva UC, Salvador C, Chesman C. Effect of doping and sintering in structure and magnetic properties of the diluted magnetic semiconductor ZnO:Ni. Ceramica. 2018;64(372):627-31. http://dx.doi.org/10.1590/0366-69132018643722463.
33. Adekunle AS, Oyekunle JAO, Oluwafemi OS, Joshua AO. Comparative catalytic properties of Ni (OH) 2 and NiO Nanoparticles Towards the Degradation of Nitrite (NO 2-) and Nitric Oxide (NO). Int J Electrochem Sci. 2014;9(2):3008-21.
34. Fechine PBA, Silva EN, de Menezes AS, Derov J, Stewart JW, Drehman AJ, et al. Structure and vibrational properties of GdIG X : YIG 1 À X ferrimagnetic ceramic composite. J Phys Chem Solids. 2009;70:202-9. http://dx.doi.org/10.1016/j.jpcs.2008.10.008.
35. Anandan K, Rajendran V. Materials science in semiconductor processing morphological and size effects of NiO nanoparticles via solvothermal process and their optical properties. Mater Sci Semicond Process. 2011;14(1):43-7. http://dx.doi.org/10.1016/j.mssp.2011.01.001.
36. Vladár AE, Hodoroaba V. Characterization of nanoparticles by scanning electron microscopy. USA: Elsevier Inc., 2020. http://dx.doi.org/10.1016/B978-0-12-814182-3.00002-X.
37. Nedumkallel AS, Sabu B, Varghese T. Effect of calcination temperature on the structural and optical properties of nickel oxide nanoparticles. Nanosyst: Phys Chem Math. 2014;5(3):441-9.
38. Peña-Garcia R, Delgado A, Farias BVM, Martinez D, Skovroinski E, Galembeck A. Magnetic and structural properties of Zn-doped yttrium iron garnet nanoparticles. Apllic Mater Sci. 2016;213(9):2485-91. http://dx.doi.org/10.1002/pssa.201533078.
39. Bertotti G. Hysterisis in magnetism. Cambridge: Academic Press; 1998. Magnetization curves; p. 297-346. http://dx.doi.org/10.1016/B978-012093270-2/50059-3.
40. Vosough M, Sharafi S, Khayati GR. Co-TiO2 nanoparticles as the reinforcement for Fe soft magnetic composites with enhanced mechanical and magnetic properties via pulse electrodeposition. Int J Eng. 2020;33(10):2030-8. http://dx.doi.org/10.5829/ije.2020.33.10a.21.
41. Peña-Garcia R, Delgado A, Guerra Y, Duarte G, Gonzales LAP, Padrón-Hernández E. The synthesis of single-phase yttrium iron garnet doped zinc and some structural and magnetic properties. Mater Res Express. 2016;4(1):016103. http://dx.doi.org/10.1088/2053-1591/aa557a.
42. Guruvammal D, Selvaraj S, Sundar SM. Effect of Ni-doping on the structural, optical and magnetic properties of ZnO nanoparticles by solvothermal method. J Alloys Compd. 2016;682:850-5. http://dx.doi.org/10.1016/j.jallcom.2016.05.038.
43. Hanish HH, Edrees SJ, Shukur MM. The effect of transition metals incorporation on the structural and magnetic properties of magnesium oxide nanoparticles. Int J Eng Trans A: Basics. 2020;33(4):647-56. http://dx.doi.org/10.5829/IJE.2020.33.04A.16.
44. Rivas J, Vaqueiro P, Caeiro D. Particle size effects on magnetic properties of yttrium iron garnets prepared by a sol – gel method. J Magn Magn Mater. 2002;247:92-8.
45. Puspitasari P, Budi LS. Physical and magnetic properties comparison of cobalt ferrite nanopowder using sol-gel and sonochemical methods. Int J Eng Trans B: Appl, 2020;33(5):877-84. http://dx.doi.org/10.5829/IJE.2020.33.05B.20.